



1 **O₃-precursor relationship over multiple patterns of time scale:**

2 **A case study in Zibo, Shandong Province, China**

3 Zhensen Zheng¹, Kangwei Li^{2*}, Bo Xu³, Jianping Dou⁴, Liming Li¹, Guotao Zhang¹,
4 Shijie Li¹, Chunmei Geng¹, Wen Yang¹, Merched Azzi⁵, Zhipeng Bai^{1*}

5
6 ¹ State Key Laboratory of Environmental Criteria and Risk Assessment, Chinese
7 Research Academy of Environmental Sciences, Beijing 100012, China
8 ² Univ Lyon, Université Claude Bernard Lyon 1, CNRS, IRCELYON, F-69626
9 Villeurbanne, France
10 ³ Zibo Eco-Environmental Monitoring Center, Zibo 255000, China
11 ⁴ Zibo Ecological Environment Quality Control Service Center, Zibo 255095,
12 China
13 ⁵ New South Wales Department of Planning, Industry and Environment, PO Box 29,
14 Lidcombe, NSW 1825, Australia

15 ***Corresponding authors:**

16 Kangwei Li (likangweizju@foxmail.com); Zhipeng Bai (baizp@craes.org.cn)
17
18

19 **Abstract.** In this study, we developed an approach that integrating multiple patterns
20 of time scale for box modeling (MCMv3.3.1) to better understand the O₃-precursor
21 relationship through multiple-site and continuous observations. A five-month field
22 campaign was conducted in the summer of 2019 to investigate the ozone formation
23 chemistry at three sites in a major prefecture-level city (Zibo) in Shandong province of
24 northern China. It was found that the relative incremental reactivity (RIR) of major
25 precursor groups (e.g., anthropogenic volatile organic compound (AVOC), NO_x) were
26 overall consistent along with time scale (four patterns: five-month, monthly, weekly,
27 and daily) varied from wider to narrower, though the magnitude of RIR varied at each
28 site. The time series of the photochemical regime (using RIR_{NO_x}/RIR_{AVOC} as indicator)
29 in weekly or daily patterns further showed varied magnitude but a synchronous
30 temporal trend among the three sites. The derived RIR ranking (top 10) of individual
31 AVOC species showed consistency at three averaged patterns (i.e., five-month, monthly,
32 and weekly). It was further found that the campaign-averaging photochemical regimes
33 showed overall consistency but non-negligible variability among the four patterns of
34 time scale, which was mainly due to the embedded uncertainty in model input dataset
35 when averaging individual daily pattern into different timescales. This implies that
36 integrating multiple patterns of time scale is useful to derive reliable and robust O₃-
37 precursor relationship. Our results highlight the importance of quantifying the impact



38 of different time scales to constrain the photochemical regime, which can formulate
39 more accurate policy-relevant guidance for O₃ pollution control.

41 1 Introduction

42 Since 2013, the ambient PM_{2.5} concentration in China has dramatically declined
43 by implementing Clean Air Action (Lu et al., 2018; Wang et al., 2020b; Zhang et al.,
44 2019). However, national ground surface ozone concentrations increased over the same
45 period (Xue et al., 2020) and became a major air quality problem that needed to be
46 addressed in China (Li et al., 2019; Wang et al., 2019). It is well-known that ground
47 surface ozone is formed mainly by complex nonlinear photochemical oxidation of
48 volatile organic compounds (VOCs) in the presence of nitrogen oxides (NO_x = NO +
49 NO₂) and sunlight (Blanchard, 2000; Hidy, 2000; Kleinman, 2000), which adversely
50 influences human health, vegetation and crops (Brunekreef and Holgate, 2002;
51 Vingarzan, 2004).

52 Given the non-linearity of ozone pollution and complex process involved in it,
53 challenges in mitigating its severity lies primarily in comprehensively understanding of
54 O₃-precursor relationship (Su et al., 2018a; Tan et al., 2018a). It is commonly
55 recognized that regional-scale air quality models and the 0-D box model are two
56 mainstream approaches to investigate the increasingly severe ozone problem
57 (Blanchard, 2000; Cardelino and Chameides, 1995; Hidy, 2000; Liu et al., 2019). The
58 0-D box model is an advanced observation-based model that implemented with gas-
59 phase chemical mechanism, and has been widely used to diagnose O₃-precursor
60 relationship in various locations (Liu et al., 2021a; Sun et al., 2016; Tan et al., 2019b;
61 Xue et al., 2014a; Yu et al., 2020a). Our recent study (Li et al., 2021) has found a large
62 variability of O₃-precursor relationship in spatiotemporal scales at Zibo, China based
63 on a July 2019 field campaign, and this phenomenon may occur widely in many other
64 cities (Lu et al., 2010; Lyu et al., 2016), which challenges current O₃ pollution control
65 (Wang et al., 2017a; Xue et al., 2014b).

66 **Table 1** summarizes the published studies of O₃-precursor relationship using the
67 0-D box model (implemented with different gas-phase chemical mechanisms) at
68 diversified patterns of time scale in many places of China. The observational period in
69 most previous studies was short-term (i.e., less than one month), while medium-term
70 (i.e., from one to several months), and long-term (i.e., multiple years) periods were
71 limited. As shown in **Table 1**, we find that model input datasets with different
72 timescales have been employed in previous studies to identify the campaign-averaging
73 O₃ formation regime, but there is a lack of comparison among these different timescales.
74 We also find that there are more than half cases using the averaged diurnal patterns as
75 box model input, which is particularly common for those medium and long-term



measurements. For example, a 10 years long-term observational study by Wang et al., (2017a) applied monthly pattern of time scale for model simulation with the reason for saving computational resources, and it also revealed a substantial temporal variability of O₃-precursor relationship. In addition, it is believed that long-term (measurements of at least several months) and multiple-site continuous online measurements can provide opportunity to develop O₃ control strategy more comprehensively over a wider spatiotemporal scale (Li et al., 2021; Wang et al., 2017b; Wang et al., 2017b). However, such measurements have been quite rare in China, limiting the present understanding of O₃-precursor relationship (Lu et al., 2019; Wang et al., 2017b).

In this study, a five-month field campaign was conducted in the summer of 2019 to investigate the ozone formation chemistry at 3 sites in Zibo, a major prefecture-level Chinese city in Shandong province. According to our measurements at the three sites in Zibo, the averaged O₃ concentration during the whole observational period was around 50 ppbv, while the daily maximum of O₃ concentrations for some extremely polluted periods were nearly 120-150 ppbv (see details in **Section 3.1**). Here we developed an approach that integrating multiple patterns of time scale for box model simulation, which aimed at illustrating the non-linearity of O₃-precursor relationship driven by its actual daily / weekly / monthly variability. Our results can be conducive to interpreting variations of O₃-precursor relationship over a wider spatiotemporal scale, and they provide implications for developing more precise and constrained O₃ control strategies in other regions.

2 Methods

2.1 Study sites and measurements

Field measurements were conducted in a major prefecture-level city (Zibo), which is in the middle of Shandong Province, northern China, from 1 May to 30 September, 2019. **Figure S1** shows the surrounding environment and geographical locations at the three sampling sites; a detailed description of the Tianzhen (TZ), Beijiao (BJ) and Xindian (XD) sites can be found in our previous study (Li et al., 2021). Briefly, TZ contains a mixture of crude oil processing and operation stations and farming areas, and is classified as suburban area; XD contains a mixture of residential and heavy industrial zones, and is considered as a suburban area; BJ is in the urban area of Zibo.

Two online gas chromatography–flame ionisation detector (GC-FID, Thermo Scientific GC5900) systems and one online gas chromatography–flame ionisation detector/photoionisation detector (GC-FID/PID, Syntech Spectras GC 955-615/815) system were deployed at TZ, BJ, and XD respectively. These GC systems measured 55 VOC species at a 1-h resolution, and detailed descriptions were given in our previous study (Li et al., 2021). Typical inorganic gases of O₃, NO, NO₂, CO and SO₂ were measured using online commercial gas analysers (Thermo Scientific 49i, 42i, 48i and



43i, USA) at the three sites. Meteorological data (i.e., temperature, relative humidity, UV-A solar radiation, precipitation, wind speed, and wind direction) were continuously monitored by the Zibo Eco-Environmental Monitoring Center at the three sites.

Table S1 summarized the limit of detection, accuracy, precision of the instruments at the three sites, and all the measurement instruments were regularly subjected to the service of checking and maintenance during the whole campaign. As for VOC measurement, two online gas chromatography–flame ionisation detector (GC-FID, Thermo Scientific GC5900) systems were automatically operated with a time resolution of 1 h at TZ and BJ sites, and measured VOC species were separated into C₂–C₅ and C₆–C₁₂ VOCs. For C₂–C₅ VOCs, a GC with pre-concentration is used by desorption and separation on a combination of two columns respectively, then a FID detector is applied for quantification. For C₆–C₁₂ VOCs, air samples are pre-concentrated on Tenax GR and subsequently separated by chromatographic column, then detected by another FID detector.

Similarly, one online gas chromatography–flame ionisation detector/photoionisation detector (GC-FID/PID, Syntech Spectras GC 955-615/815) system was deployed with time resolution of 1 h at XD site. For C₂–C₆ VOCs, the hydrocarbons are concentrated on a Tenax GR carrier, then thermally desorbed and separated on a DB-1 column, and finally detected by FID and PID detectors. For C₆–C₁₂ VOCs, the air sample is concentrated on a Carbosieves SIII carrier at 5°C, then thermally desorbed and separated on a system consisting of two columns, and FID and PID detectors are employed for subsequent detection. More details of online VOC measurement also can be found elsewhere (Chien, 2007; Jiang et al., 2018; Xie et al., 2008).

To ensure the quality assurance / quantity control (QA/QC) of online VOC measurement, two five-point calibrations (i.e., 2, 4, 6, 8, 10 ppbv) for standard gases with 55 VOC species (Linde Co., Ltd, USA) were carried out in May and August of 2019 at the three sites. **Table S2** showed that the calibration linearity (R^2) of all measured VOCs were nearly 0.9990. Additionally, a single-point calibration (i.e., 6 ppbv) was regularly performed every month during the whole campaign. As shown in **Figure S2** (a case from TZ), the retention time, peak fitting and baseline of the total ion current (TIC) chromatogram were manually checked and adjusted on a daily basis.

2.2 0-D box model and design of four patterns of time scale

The 0-D box model integrated with the latest Master Chemical Mechanism of MCMv3.3.1 (<http://mcm.york.ac.uk/>) has been widely utilized in many regions (He et al., 2019; Jenkin et al., 2015; Liu et al., 2019; Whalley et al., 2021). Unlike the lumped chemical mechanisms such as CB05 (Wang et al., 2017a; Yarwood et al., 2005), CB6 (Yarwood et al., 2010), RACM/RACM2 (Goliff et al., 2013; Stockwell et al., 1997,



2020) and SAPRC-07 (Carter, 2010), the MCMv3.3.1 is a near-explicit chemical mechanism consisting of over 5,800 species and 17,000 reactions (Jenkin et al., 2015; Saunders et al., 2003), which can be used to describe the gas-phase chemistry (i.e., in-situ photochemistry). In this study, the box model (F0AM) (Wolfe et al., 2016) was applied and constrained by the mean diurnal profiles of meteorological data (i.e., temperature, relative humidity, and photolysis rates), 4 inorganic gases (i.e., SO₂, CO, NO, and NO₂), and 45 speciated VOCs (in the VOC species list of MCMv3.3.1; see **Table S3**). Since measured photolysis rates (*J* values) were not available, the measured UV-A solar radiation was used to scale the photolysis rates calculated from the Tropospheric Ultraviolet and Visible Radiation model (TUVv5.2; https://www.acom.ucar.edu/Models/TUV/Interactive_TUV/) following the approach of recent studies (Lyu et al., 2019; Lyu et al., 2016). A dilution rate of 3/86400 s⁻¹ was applied for all non-constraint species and simulation days through a stepwise sensitivity test by adjusting it from 1/86400 s⁻¹ to 5/86400 s⁻¹ (see details in **Text S3**). For each model run (i.e., each daily model simulation), it was performed on a daily basis with intervals of 24 hours spanning from 0:00 to 23:00, and each individual model simulation was run to reach one-day diurnal steady state. The detailed descriptions of box model operation were provided in our previous study (Li et al., 2021).

Since the box model simulations are conducted with intervals of 24 hours spanning from 0:00 to 23:00 local standard time (Wang et al., 2018), the entire campaign observations were taken into four patterns of time scale (i.e., five-month, monthly, weekly, and daily) as diurnal average format for model input (**Figure 1**). Note that some days or weeks were not modeled due to significant miss in the measurements. Nevertheless, the total simulation number at the daily (i.e., 100, 81, and 114 days for TZ, BJ and XD respectively) or weekly (i.e., 21, 20, and 19 weeks for TZ, BJ, and XD respectively) scale was representative of the five-month campaign. Specifically, the entire campaign dataset was processed into four patterns of time scale, and were modeled as base runs. Then we performed the sensitivity modeling to calculate the relative incremental reactivity (RIR) of precursors by adjusting the input concentrations in the base runs (see next section) (Lu et al., 2010a).

2.3 Calculation of net O_x production rate *P*(O_x) and Relative incremental reactivity (RIR)

Considering the rapid chemical titration of NO to NO₂ in the presence of O₃, the concept of ‘total oxidant’ (O_x = O₃ + NO₂) has been widely used to represent the actual photochemical production of O₃ (Lu et al., 2010). Similar to those described in previous studies using the 0-D box model (He et al., 2019; Lyu et al., 2016), the net or in-situ O_x production rate (*P*(O_x)) is defined as the difference between the O_x gross production rate (*G*(O_x)) and the O_x destruction rate (*D*(O_x)), which is formulated in accordance



with Eq. (1):

$$P(O_x) = G(O_x) - D(O_x) \quad (1)$$

The O_x gross production rate ($G(O_x)$), or the total chemical production of O_x , is calculated by summing the rates of oxidation of NO by HO_2 and RO_2 radicals in accordance with Eq. (2):

$$G(O_x) = k_{HO_2+NO}[HO_2][NO] + \sum k_{RO_{2,i}+NO}[RO_{2,i}][NO] \quad (2)$$

The O_x destruction rate ($D(O_x)$), or total chemical loss of O_x , is calculated by summing O_3 photolysis, the reaction of O_3 with OH, HO_2 and alkenes, as well as the reaction between NO_2 and OH, as described by Eq. (3):

$$D(O_x) = k_{O^1D+H_2O}[O^1D][H_2O] + k_{OH+O_3}[OH][O_3] + k_{HO_2+O_3}[HO_2][O_3] + k_{alkenes+O_3}[alkenes][O_3] + k_{OH+NO_2}[OH][NO_2] \quad (3)$$

Concentrations of radicals and intermediates are obtained from the outputs of the 0-D box model. The k values in Eq. (2) and (3) represent the rate constants of the corresponding reactions, respectively. The subscript 'i' in Eq. (2) represents the individual RO_2 species.

Additionally, relative incremental reactivity (RIR) has been widely used as a metric to quantify the O_3 -precursor relationship, and it can be derived from the 0-D box model (MCMv3.3.1) by changing the input mixing ratios of its precursors (Sillman, 2010; Xue et al., 2014a). The RIR is defined as the ratio of percentage change in net O_x ($O_x = O_3 + NO_2$) production rate $P(O_x)$ (Li et al., 2021) to percentage change of concentration of precursor X. The RIR of a specific precursor X is described in Eq. (4):

$$RIR(X) = \frac{[PO_x(X) - PO_x(X - \Delta X)] / PO_x(X)}{\Delta C(X) / C(X)} \quad (4)$$

Here, X is a specific precursor (i.e., NO_x , CO or grouped / individual VOC species), $C(X)$ is the measured concentration of precursor X, and $\Delta C(X)$ is the concentration change caused by the hypothetical change (ΔX , 10% of X in this study in accordance with the previous studies (Lyu et al., 2016; Wang et al., 2018)) in precursor X. Therefore, $\Delta C(X) / C(X)$ was 10% in this study. $PO_x(X)$ represents the simulated O_x production rate in a base run, whereas $PO_x(X - \Delta X)$ is the simulated O_x production in a second run with a hypothetical concentration change (10%) of species X. Obviously, a higher positive value of $RIR(X)$ suggests a more effective way of reducing the ambient O_3 production rate by reducing X (Ling et al., 2011; Zhang et al., 2008a). In this study, the RIR method was applied mainly to evaluate the O_3 - NO_x -VOC sensitivity and determine the photochemical regimes among four patterns of time scale.



223 3 Results and discussion

224 3.1 Overview of the field campaign

225 **Figure 2** shows the time series of measured meteorological parameters and O₃ as
226 well as its precursors at the three sites during the whole campaign. In general, the
227 temperature (*T*) and relative humidity (RH) were basically consistent at the three sites,
228 while the wind speeds were different, which suggests that the three sites had an overall
229 consistent meteorological condition. In addition, the time series of UV-A radiation was
230 shown in **Figure 2d**, which was only available from one urban site of Zibo but expected
231 to represent the whole Zibo city in this study. Following the protocol of the previous
232 studies (Lyu et al., 2019; Wang et al., 2017b; Xue et al., 2014), the time series of
233 photolysis rates (e.g., J_{NO₂} (**Figure 2e**) and J_{O¹D} (**Figure 2f**)) were calculated from
234 TUVv5.2 model and further scaled from UV-A radiation measurement.

235 As shown in **Figure 2g**, we found that severe O₃ pollution was observed at the
236 three sites throughout the whole campaign. According to our measurements at the three
237 sites in Zibo, the averaged O₃ concentration during the whole observational period was
238 around 50 ppbv, while the daily maximum of O₃ concentrations for some extremely
239 polluted periods were nearly 120-150 ppbv (**Figure 2g**). Interestingly, the O₃
240 concentrations at the three sites were generally consistent, while the levels of its
241 precursors (e.g., VOC, NO_x) were obviously different (**Figure 2h-k**), which implies
242 the site-to-site variation of O₃ formation chemistry for the whole Zibo city.

243 Generally, OH reactivity (or OH loss rate, *k*_{OH}) is widely applied to quantify the
244 capacity of OH consumption by VOCs (Tan et al., 2019a). According to **Table S3**, the
245 BVOC reactivity (*k*_{BVOC}, 3.5 ± 4.1 s⁻¹) in TZ were highest within the three sites. As BJ
246 was mainly influenced by the emission from urban region, it showed the highest AVOC
247 reactivity (*k*_{AVOC}, 6.8 ± 6.3 s⁻¹) and NO_x level (31.1 ± 28.6 ppbv). In addition, XD
248 showed the highest level of alkenes* reactivity (anthropogenic alkenes which excludes
249 isoprene in this study) of 4.0 ± 3.2 s⁻¹ within the three sites, and the local petrochemical
250 industry nearby XD area may explain such characteristic (Li et al., 2021).

251 3.2 Evaluation of box model performance

252 The measured O₃ concentrations were not constrained in our MCMv3.3.1 box
253 model calculation, thus the model performance could be quantitatively assessed by
254 comparing the modeled O₃ (from base runs) with the measured O₃. **Figure S3-S8** show
255 the time series of simulated and observed O₃ concentrations at four patterns of time
256 scale. In most cases, the box model simulation could accurately capture the level and
257 variation trend of the observed O₃. However, on some days the modeling results
258 underestimated or overestimated the O₃ concentrations. Such discrepancies between the
259 simulated and observed O₃ were likely due to limitations in explicit representations of



atmospheric and transport processes (i.e., the horizontal and vertical transport process of ground ozone) by 0-D modeling approach (Lyu et al., 2019; Yu et al., 2020b). Specifically, ozone simulated by the 0-D box model is considered as in-situ photochemical processes from its precursors. Unlike the 3-D air quality model, 0-D box model usually simplifies the representation of the physical processes (i.e., deposition and advection) (Lu et al., 2010a; Sillman, 2010). Note that some adjustable parameters (e.g., radiation scheme, dilution rate) were remained consistent in all of our model calculations, which ensured the comparability of model results to the greatest extent.

The index of agreement (*IOA*) (Li et al., 2021; Lyu et al., 2016), Pearson's correlation coefficient (*r*) and root mean square error (*RMSE*) were jointly used as statistical metrics to quantify the goodness-of-fit between the simulated and observed O_3 concentrations. **Table S4** summarizes these statistical metrics for each site at various patterns of time scale. Because any single statistical metric has its own limitations, using these three indicators conjointly provided a more comprehensive evaluation of the model performance (Su et al., 2018b). Generally, higher *IOA* and *r* as well as lower *RMSE* indicate better agreement between the simulated and observed values (Wang et al., 2018; Willmott, 1982). As shown in **Table S4**, slightly reduced correlation was observed as the time scale changed from the wider (i.e., five-month scale) to the narrower (i.e., daily scale) pattern, which is understandable because of the enlarged statistical samples in the narrower pattern of time scale.

In summary, TZ showed the best performance of the box model simulation, followed by XD and BJ, regardless of any statistical metrics or different patterns of time scale. The overall model performance in this study (i.e., a day-to-day *IOA* of approximately 0.90 for TZ) was close to or slightly better than those reported in previous studies, such as *IOA* = 0.74 in Hong Kong (Liu et al., 2019), *IOA* = 0.74 in Wuhan (Lyu et al., 2016) and *IOA* = 0.90 in Jiangmen (He et al., 2019). According to the above evaluation of base runs, our modeled results were acceptable for the subsequent O_3 -precursor relationship analysis described in the following sections.

3.3 Month-to-month

The O_3 precursors were divided into four major categories, including anthropogenic VOC (AVOC), biogenic VOC (BVOC, only isoprene in this study), CO and NO_x (Tan et al., 2019b). AVOC was further divided into three subcategories: alkanes, aromatics and alkenes* (the asterisk denotes anthropogenic alkenes, excluding isoprene in this study) (Yu et al., 2020a). Additionally, the RIR values of major precursor groups (i.e., AVOC, BVOC, CO, NO_x , alkanes, alkenes* and aromatics) were calculated to further quantify the O_3 -precursor relationship (see section 2.3 for more details). **Figure 3a-b** presents the monthly RIR values of the major precursor groups at each site, and the large variability of O_3 -precursor relationship at spatiotemporal scale (i.e., site-to-



site and month-to-month) was observed. Specifically, in most months, XD generally showed the highest RIR_{AVOC} among the three sites, followed by BJ and TZ. In addition, RIR_{BVOC} showed similar level to RIR_{AVOC} in TZ, but much less than RIR_{AVOC} in BJ and XD, which can be explained by the observed higher BVOC reactivity in TZ than the other two sites (see **Figure S13** and **Table S3**). Also, almost all the precursor groups showed positive RIR values, except negative RIR_{NO_x} appeared in BJ and XD in September. Among the three subcategories of AVOC, alkenes* always had the highest RIR values, followed by aromatics, while the contribution of alkanes to O_3 formation can be ignored due to their near-zero RIR values. That sequence of O_3 -AVOC sensitivity (alkenes* > aromatics > alkanes) indicated by the RIR analysis was consistent with previous studies in some other Chinese cities (Su et al., 2018b; Tan et al., 2019b). Significant monthly variations of O_3 , NO_x , CO, VOC reactivity and TVOC/ NO_x ratios (in ppbC/ppbv, as a widely used simple metric to determine the photochemical regime) (National Research Council, 1991) were also observed from May to September (see **Figure S13** and **Table S3**) at the three sites, which indicates the temporal variation of local primary emission for O_3 precursors.

O_3 formation chemistry is usually classified into two regimes (i.e., VOC-limited and NO_x -limited) or three regimes (i.e., VOC-limited, transitional and NO_x -limited) (He et al., 2019; Wang et al., 2018). In this study, RIR_{NO_x}/RIR_{AVOC} (the ratio of two RIR values) was used as a metric to classify the photochemical regimes (Li et al., 2021). Specifically, RIR_{NO_x}/RIR_{AVOC} value of less than 0.5 was defined as VOC-limited regime, greater than 2 as NO_x -limited regime, and from 0.5 to 2 as transitional regime (see **Text S2** and **Table S5**) (Li et al., 2021). **Figure 3c** shows monthly RIR_{NO_x}/RIR_{AVOC} at each site, which clearly reveals the spatial and temporal variations in photochemical regimes. For instance, the photochemical regime at the TZ site was considered to be transitional regime in May, NO_x -limited regime in June and July, and VOC-limited regime in August and September; whereas for a specific month like June, NO_x -limited, VOC-limited, and transitional regimes were generally identified for TZ, BJ, and XD respectively. **Figure 5b** shows good consistency between monthly TVOC/ NO_x and RIR_{NO_x}/RIR_{AVOC} , suggesting that the changes of local emissions for O_3 precursors may explain the considerable variation of O_3 formation chemistry in different months.

3.4 Week-to-week

Figure 4 shows the time series of week-to-week RIR values of major precursor groups and RIR_{NO_x}/RIR_{AVOC} at three sites in Zibo. Compared with month-to-month results, **Figure 4** further reveals the O_3 -precursor relationship with more information in temporal trends. The temporal variations in weekly RIR_{AVOC} at the three sites generally decreased and then increased, whereas weekly RIR_{NO_x} represented an opposite temporal variation during the entire campaign. Additionally, weekly RIR_{BVOC} showed a trend of



first decrease and then increase at TZ, while it did not show clear temporal variation at BJ and XD due to low values (**Figure 4a-c**). In general, $RIR_{alkanes}$, $RIR_{alkenes^*}$ and $RIR_{aromatics}$ showed a tendency consistent with that of the RIR_{AVOC} at three sites (**Figure 4d-f**). Overall, these phenomena were consistent among the three sites, though the magnitude of RIR values varied site-to-site. In parallel, the temporal changing of O_3 precursor (e.g., AVOC, NO_x) was also observed at the three sites during the entire campaign (see **Figure S14**). For example, the weekly NO_x concentration showed an overall trend of first decrease and then increase, while the AVOC reactivity showed a different temporal variation. Given the good consistency between weekly TVOC/ NO_x and RIR_{AVOC}/RIR_{NO_x} (**Figure 5c**), the temporal variations of RIR values and O_3 formation chemistry at the three sites may be elucidated by the emission changes of O_3 precursors.

As shown in **Figure 4g-i**, all the three sites showed similar temporal trends of RIR_{NO_x}/RIR_{AVOC} , as it increased first and then decreased, though the magnitude of RIR_{NO_x}/RIR_{AVOC} varied largely at each site. Such site-to-site variability of RIR_{NO_x}/RIR_{AVOC} suggests that the photochemical regime in a local scale was mainly influenced by local emissions. By contrast, the site-to-site synchronization in temporal trend of RIR_{NO_x}/RIR_{AVOC} suggests that the photochemical regime in a local scale may also be influenced by the emissions in a regional area. Therefore, the long-term, week-to-week RIR_{NO_x}/RIR_{AVOC} of multiple sites can further reflect the variability of ozone formation regime at a large geographic scale.

3.5 Day-to-day

In this section, O_3 -precursor relationship at the narrowest pattern of time scale was identified in detail. **Figure S9-S10** shows the time series of daily RIR values at three sites in Zibo, where the temporal trend of RIR values was consistent with that at weekly scale (**Figure 4**). Additionally, the time series of daily RIR_{NO_x}/RIR_{AVOC} (**Figure S11**) first increased and then decreased during the entire campaign, which was also consistent with that of weekly scale. In summary, the time series of RIR values from the daily scale can provide more informative variations and characteristics of O_3 -precursor relationship in temporal trends.

Table 2 summarizes the number of days and proportions that were classified into the three photochemical regimes across each site and each pattern of time scale. Near-consistent proportions of O_3 formation regimes (using RIR_{NO_x}/RIR_{AVOC} as a metric) were shown among multiple patterns of time scale, whereas a variability of proportion occurred among the three sites. The proportions of photochemical regimes changed accordingly along with the time scale varied from wider to narrower pattern. Taking TZ as an example, 20% (monthly) and 26% (daily) of the time was considered as VOC-limited regime. The number of days and proportions for photochemical regimes



summarized at four patterns of time scales can reveal a more plausible and comprehensive variation in ozone formation chemistry. Compared with patterns of monthly and weekly scales, the results derived at a daily scale can reveal the temporal variability of photochemical regimes more comprehensively. Note that the photochemical regime proportion obtained from the day-to-day scale has an advantage due to the large number of statistical samples.

3.6 Comparison among different patterns of time scale

This section gives a more comprehensive understanding of the campaign-averaging O₃-precursor relationship by comparing the similarities and differences of the results from various patterns of time scale. The overall O₃-precursor relationship for the entire campaign can be quantified by averaging the RIR values from the individual simulation runs depending on the chosen time scale (e.g., five simulation runs for monthly scale in this study). Therefore, four sets of logical and comparable results can be derived to represent the campaign-averaging O₃-precursor relationship, as four patterns of time scale (i.e., five-month, monthly, weekly, and daily) were treated in this study.

Figure 6 shows the averaged RIR values of the major precursor groups at different patterns of time scale. As the time scale changed from wider (i.e., five-month scale) to narrower (i.e., daily scale) pattern, all three sites showed increased RIR_{AVOC} and RIR_{alkenes*} as well as decreased RIR_{NO_x}, whereas the RIR of other precursors (i.e., BVOC, CO, alkanes and aromatics) did not vary obviously (see **Table S6**). Comparing the O₃-VOC-NO_x sensitivity at the daily scale, the results obtained at the five-month scale underestimated O₃-AVOC sensitivity by 48% (TZ), 66% (BJ), and 49% (XD), and overestimated O₃-NO_x sensitivity by 37% (TZ), 142% (BJ), and 144% (XD). We performed comprehensive uncertainty analysis for model input and output results, which was assessed through statistical methods (see details in **Section 3.7**). We found that the model-derived RIR values may become more uncertain when the input dataset was averaged into a wider diurnal pattern (i.e., five-month scale), which may explain the discrepancy of RIR values between five-month scale and daily scale. We expect that such discrepancies derived from different patterns of time scale could widely exist in many other world areas. Note that the mean RIR values were generally consistent among the four patterns of time scale within a reasonable range (within 25-75th quantile and standard deviation, see **Figure 6** and **Table S5**), suggesting that any selected pattern of time scale could reasonably derive the campaign-averaging O₃-precursor relationship.

Figure 7 further shows the variations in photochemical regimes (defined by RIR_{NO_x}/RIR_{AVOC}; see **Text S2** and **Table S5** for details) for each pattern of time scale. Specifically, TZ was mainly considered as transitional regime for the entire campaign period, whereas its variations covered three photochemical regimes, which was



consistent with the results from **Table S6**. BJ was generally identified as VOC-limited regime, whereas some days were also grouped into transitional regime. XD was considered as primarily between VOC-limited and transitional regime, and its variations also spanned three photochemical regimes. Compared with the five-month pattern, it was further found that the averaged RIR_{NOx}/RIR_{AVOC} from other time scale patterns (i.e., monthly, weekly, and daily) were higher (12% to 20% for TZ; 38% to 153% for XD) or lower (21% to 65% for BJ) than that from five-month scale. Note that the above discrepancies in photochemical regime derived from multiple patterns of time scale may influence the development of targeted O_3 control strategies. In summary, the photochemical regime derived by averaging RIR_{NOx}/RIR_{AVOC} from the daily scale (see **Table S6**) suggests that the three sites mainly followed the sequence of TZ (1.34 ± 1.39) > XD (0.67 ± 1.49) > BJ (0.16 ± 0.65).

In addition, the temporal variations of TVOC/ NO_x in different timescales were identified during the whole campaign, and good correlations between observed TVOC/ NO_x and model derived RIR_{NOx}/RIR_{AVOC} at four patterns of time scale were also found (see **Figure 5**). Such consistency suggests that both metrics can reasonably reflect the variation of photochemical regimes, which can also improve the reliability of our box model simulation.

The consistency and difference of model output (summarized in **Table S7**) are quantified by the statistical methods of Pearson's correlation coefficient (Hu et al., 2018) and paired-samples *t*-test analysis (Wang et al., 2016). In particular, we assess and compare the degree of significance of differences among multiple patterns of time scale by the *p* values (a statistical significance assuming at $p < 0.05$) through paired-samples *t*-test and Wilcoxon matched-paired signed-rank test (non-parametric statistics) (Chiclana et al., 2013). **Figure 8a** shows high Pearson's correlation coefficients (with values all above 0.85, $p < 0.01$) were found among four patterns of time scale, and the higher correlation coefficient was identified between the two closer patterns. **Figure 8b-c** shows that the differences among multiple patterns of time scale were non-significant using Paired-samples *t*-test analysis and Wilcoxon matched-pair signed-rank test respectively. Furthermore, their results indicate that more significant difference was recognized between the two distant patterns (e.g., daily and five-month), which is consistent with the results of Pearson's correlation analysis. Noted that the discrepancy between the two distant patterns was not significant but non-negligible (e.g., $p = 0.092$ of Wilcoxon matched-paired signed-rank test between five-month and daily patterns).

The influence of different patterns of time scale on deriving RIR values from individual AVOC species was further investigated. Briefly, quantifying the relative contribution of individual AVOC on O_3 formation based on RIR calculation is beneficial to the development of cost-effective AVOC control strategies (Zhang et al., 2021). **Figure 9** shows the averaged RIR values of individual AVOC species (i.e., top 10) at



different patterns of time scale (i.e., five-month, month-to-month, week-to-week) at three sites in Zibo. As shown in **Figure 9**, the 10 individual AVOC species at the three sites were selected according to the top 10 highest RIR from five-month pattern. All three sites showed that the RIR of individual AVOC species increased gradually as the time scale changed from the wider (i.e., five-month) to narrower (i.e., weekly) pattern, which was consistent with the earlier discussion (see **Figure 6** and **Table S6**) of O₃-AVOC sensitivity derived from four patterns of time scale. The results also indicate that the choice of time scale pattern has a limited effect on deriving high-ranking AVOC species (i.e., top 10) based on RIR calculations.

3.7 Uncertainty analysis

The uncertainty of model input comprehensively was assessed and quantified in this section, which is embedded in pre-processed dataset with multiple patterns of time scale. The box model simulation was performed on a daily basis with intervals of 24 hours spanning from 0:00 to 23:00 local standard time. As showed in **Figure 1**, the daily simulation used the individual daily pattern to constrain model, while the input dataset of averaged diurnal patterns (i.e., weekly, monthly, and five-month) is treated by averaging individual daily pattern into different timescales. Note that compared with the model input data from daily pattern, the discrepancies of O₃ precursor groups from averaged diurnal patterns (i.e., weekly, monthly, and five-month) were overall limited (see **Table S7**), which is reasonably for such kind of time series observation data. However, as shown in our analysis in previous section, the model input dataset with averaged diurnal patterns (i.e., weekly, monthly, and five-month) will result in non-negligible discrepancy and uncertainty of model output. Therefore, the standard deviation of averaged diurnal patterns was employed to quantify the uncertainty of model input dataset. **Figure 10** shows the distributions of the standard deviations for OH reactivity (k_{OH}) or concentration of O₃ precursor groups at three averaged patterns of time scale at the three sites. As the time scale changed from wider (i.e., five-month scale) to narrower (i.e., weekly scale) pattern, the uncertainty (indicated by the average, median and 25%-75% quantile of the standard deviations) decreased accordingly. Note that the 10-90% quantile of the standard deviations partly presented with different trend, which was due to the enlarged statistical samples at narrower (i.e., weekly scale) pattern. Generally, such uncertainty of model input dataset will lead to the discrepancy of model output results, especially for determining O₃ formation chemistry at the wider pattern of time scale.

Moreover, it has been widely recognized that the uncertainty for 0-D box model simulation mainly arises from the constraint of observation dataset and the configuration of model scheme. Note that constraints with more species from measurements (or including as many species as possible) would lower its uncertainty



from the chemical box model simulation (Wolfe et al., 2011, 2016). Nevertheless, due to the measurement limitation in our field campaign, we are unable to measure some important atmospheric species (i.e., HONO and oxygenated VOC (OVOC)), and these may arise uncertainty in box model simulation. For instance, Xue et al., (2021) performed a sensitivity test for HONO constraint in their box model simulation, and they showed that without HONO constraint would lead to O₃ photochemical production rate decreasing by 42%. More recently, Wang et al., (2022) obtained a comprehensive VOC dataset at Guangzhou, and their results showed that box model simulation without OVOCs constraints would underestimate the productions of RO_x and O₃. In addition, the parameter configuration of model scheme is essential to derive a reliable and valid model output. Dilution rate is an important model technical parameter, which is essential to obtain a reliable model output result. We performed a stepwise sensitivity test for this parameter to obtain an optimized dilution rate, and assigned it to all non-constraint species, which can reduce uncertainty in box model simulation (see details in **Text S3**). Also, the dry and/or wet deposition of pollutants is an important atmospheric physical process, which has been mostly parameterized in emission-based chemical transport modeling but very limited in box model, as most of the primarily emitted species are already constrained from measurements. Xue et al., (2014) considered O₃ deposition into box model simulation, and their result showed negligible contribution of O₃ deposition to total O₃ destruction rates. As for this work, we are unable to consider the deposition due to the difficulty in representing and parameterizing this term in the 0-D box model. Nevertheless, deposition of O₃ and other species may be one of the uncertainties during box model simulation, which is worth further study in the future.

4 Summary and implications

Our present results suggest that comprehensively understanding of multiple patterns of time scale is conducive to formulating a more accurate and robust O₃ control strategy. Specifically, as identified from the narrower patterns of time scale (i.e., weekly and daily), the site-to-site photochemical regime indicated by RIR_{NO_x}/RIR_{AVOC} showed various magnitudes but a synchronous temporal trend. This indicates that the O₃ formation regime in a city area can be influenced by local and regional emissions jointly. The reason behind this phenomenon is not clear at present, and we believe that further investigation on the synergetic effect of local and regional emission reduction for O₃ control would help elucidating this observation. It was also found that the campaign-averaging photochemical regimes showed overall consistency but non-negligible variability among the four patterns of time scale, which was mainly due to the embedded uncertainty in model input dataset with averaged diurnal patterns. This implies that comparison among multiple patterns of time scale based on RIR analysis



527 is useful to derive the O₃-precursor relationship more accurately and reliably.

528 Moreover, the high-ranking AVOC species (i.e., top 10) based on RIR calculations
529 were overall consistent from the narrow to wide patterns of time scale. This
530 demonstrates that datasets with wider pattern of time scale can still produce an accurate
531 RIR ranking / prioritization for VOC control. **Table S8** summarizes the total run number
532 of box model for different patterns of time scale. It is known that large-scale computing
533 capacity and computational efficiency were required in the narrower pattern of time
534 scale (e.g., 2760 simulation runs in weekly scale in this study). Considering the
535 difficulties of performing long-term and continuous online measurements in some
536 environments, it is also advisable to identify the high-ranking VOC species from the
537 campaign-averaging diurnal pattern in box model simulation.

538 In this study, we explored the non-linearity of O₃-precursor relationship in a way
539 driven by the actual daily / weekly / monthly variability around the distribution. Our
540 results highlight the importance to quantitatively test the impact of different timescales
541 on photochemical regime determination, as there is uncertainty embedded in model
542 input dataset when averaging individual daily pattern into different timescales. Such
543 understanding would be complementary in developing more accurate O₃ pollution
544 control strategy, particularly as the long-term O₃-precursor observations (e.g., from
545 several months to years) are becoming more available than before in many places of
546 China. In addition, site-to-site difference of model-derived photochemical regimes also
547 underlines the importance of developing target O₃ control strategy for different areas in
548 a city scale. Specifically, according to the averaged RIR_{NO_x}/RIR_{AVOC} at daily pattern,
549 the derived photochemical regime was transitional for TZ (suburban) and XD
550 (suburban), while VOC-limited for BJ (urban). This implies that for mitigating ozone
551 pollution in Zibo city, more endeavors should be devoted to the anthropogenic VOC
552 reduction in urban areas, while strengthening the synergetic mitigation of VOC and
553 NO_x emissions at the same time in other suburban areas. Although the above
554 implications for O₃ control were derived from a case study in a major prefecture-level
555 city (Zibo) of northern China, the developed approach by integrating multiple patterns
556 of time scale in the present work can be used to other regions, particularly the on-going
557 “One City One Policy” campaign (2021-2023) for O₃ control in many cities in China.



558 Acknowledgement

559 This work was supported by National Center for Air Pollution Prevention and Control
560 (No. DQGG202119) and Ministry of Science and Technology PRC (No.
561 G20200160001). We also thank Prof. William Bloss for helpful comments.

562 Data and code availability

563 The code for the Master Chemical Mechanism (MCMv3.3.1) can be achieved from
564 <http://mcm.york.ac.uk/>. The datasets generated during and/or analysed during the
565 current study are available from the corresponding author on reasonable request.

566 Author contribution

567 KL conceived the study; ZZ performed the modeling; ZZ, KL, and ZB analyzed the
568 data; BX, JD, LL, SL, CG, and WY conducted the field measurement; ZZ and KL wrote
569 the paper with assistance of interpretation and revision from all authors. All authors
570 contributed to the manuscript preparation and discussions.

571 Conflicts of interest

572 The authors declare that they have no conflicts of interest.

573 Supplement

574 The supplementary discussion of RIR calculation of different hypothetical changes,
575 determining the photochemical regime, sensitivity test of different dilution rates, and
576 detailed box modeling results are provided in **Text S1-S3**, **Table S1-S8** and **Figure S1-**
577 **S18**.



References

- Blanchard, C. L.: Ozone process insights from field experiments – Part III: extent of reaction and ozone formation, *Atmos. Environ.*, 34(12), 2035–2043, doi:https://doi.org/10.1016/S1352-2310(99)00458-6, 2000.
- Brunekreef, B. and Holgate, S. T.: Air pollution and health, *Lancet*, 360(9341), 1233–1242, doi:10.1016/S0140-6736(02)11274-8, 2002.
- Cardelino, C. A. and Chameides, W. L.: An observation-based model for analyzing ozone precursor relationships in the urban atmosphere, *J. Air Waste Manag. Assoc.*, 45(3), 161–180, doi:10.1080/10473289.1995.10467356, 1995.
- Carter, W. P. L.: Development of the SAPRC-07 chemical mechanism, *Atmos. Environ.*, 44(40), 5324–5335, doi:https://doi.org/10.1016/j.atmosenv.2010.01.026, 2010.
- Cheng, H., Guo, H., Wang, X., Saunders, S. M., Lam, S. H. M., Jiang, F., Wang, T., Ding, A., Lee, S. and Ho, K. F.: On the relationship between ozone and its precursors in the Pearl River Delta: Application of an observation-based model (OBM), *Environ. Sci. Pollut. Res.*, 17(3), 547–560, doi:10.1007/s11356-009-0247-9, 2010.
- Chiclana, F., García, J. M. T., del Moral, M. J. and Herrera-Viedma, E.: A statistical comparative study of different similarity measures of consensus in group decision making, *Inf. Sci. (Ny.)*, 221, 110–123, 2013.
- Chien, Y.-C.: Variations in amounts and potential sources of volatile organic chemicals in new cars, *Sci. Total Environ.*, 382(2), 228–239, doi:https://doi.org/10.1016/j.scitotenv.2007.04.022, 2007.
- National Research Council: Rethinking the Ozone Problem in Urban and Regional Air Pollution, The National Academies Press, Washington, DC., 1991.
- Fan, M. Y., Zhang, Y. L., Lin, Y. C., Li, L., Xie, F., Hu, J., Mozaffar, A. and Cao, F.: Source apportionments of atmospheric volatile organic compounds in Nanjing, China during high ozone pollution season, *Chemosphere*, 263, 128025, doi:10.1016/j.chemosphere.2020.128025, 2021.
- Goliff, W. S., Stockwell, W. R. and Lawson, C. V.: The regional atmospheric chemistry mechanism, version 2, *Atmos. Environ.*, 68, 174–185, doi:https://doi.org/10.1016/j.atmosenv.2012.11.038, 2013.
- He, Z., Wang, X., Ling, Z., Zhao, J., Guo, H., Shao, M. and Wang, Z.: Contributions of different anthropogenic volatile organic compound sources to ozone formation at a receptor site in the Pearl River Delta region and its policy implications, *Atmos. Chem. Phys.*, 19(13), 8801–8816, doi:10.5194/acp-19-8801-2019, 2019a.
- He, Z., Wang, X., Ling, Z., Zhao, J., Guo, H., Shao, M. and Wang, Z.: Contributions of different anthropogenic volatile organic compound sources to ozone formation at a receptor site in the Pearl River Delta region and its policy implications, *Atmos. Chem. Phys.*, 19(13), 8801–8816, doi:10.5194/acp-19-8801-2019, 2019b.
- Hidy, G. M.: Ozone process insights from field experiments - part I: Overview, *Atmos.*



- Environ., 34(12–14), 2001–2022, doi:10.1016/S1352-2310(99)00456-2, 2000.
- Hu, H., Landgraf, J., Detmers, R., Borsdorff, T., Aan de Brugh, J., Aben, I., Butz, A. and Hasekamp, O.: Toward global mapping of methane with TROPOMI: First results and intersatellite comparison to GOSAT, *Geophys. Res. Lett.*, 45(8), 3682–3689, 2018.
- Jenkin, M. E., Young, J. C. and Rickard, A. R.: The MCM v3.3.1 degradation scheme for isoprene, *Atmos. Chem. Phys.*, 15(20), 11433–11459, doi:10.5194/acp-15-11433-2015, 2015.
- Jiang, M., Lu, K., Su, R., Tan, Z., Wang, H., Li, L., Fu, Q., Zhai, C., Tan, Q. and Yue, D.: Ozone formation and key VOCs in typical Chinese city clusters, *Chinese Sci. Bull.*, 63(12), 1130–1141, 2018.
- Kleinman, L. I.: Ozone process insights from field experiments – part II: Observation-based analysis for ozone production, *Atmos. Environ.*, 34(12), 2023–2033, doi:https://doi.org/10.1016/S1352-2310(99)00457-4, 2000.
- Li, J., Zhai, C., Yu, J., Liu, R., Li, Y., Zeng, L. and Xie, S.: Spatiotemporal variations of ambient volatile organic compounds and their sources in Chongqing, a mountainous megacity in China, *Sci. Total Environ.*, 627, 1442–1452, 2018.
- Li, K., Jacob, D. J., Liao, H., Shen, L., Zhang, Q. and Bates, K. H.: Anthropogenic drivers of 2013–2017 trends in summer surface ozone in China, *Proc. Natl. Acad. Sci.*, 116(2), 422 LP – 427, doi:10.1073/pnas.1812168116, 2019.
- Li, K., Wang, X., Li, L., Wang, J., Liu, Y., Cheng, X., Xu, B., Wang, X., Yan, P., Li, S., Geng, C., Yang, W., Azzi, M. and Bai, Z.: Large variability of O₃-precursor relationship during severe ozone polluted period in an industry-driven cluster city (Zibo) of North China Plain, *J. Clean. Prod.*, 316, 128252, doi:https://doi.org/10.1016/j.jclepro.2021.128252, 2021.
- Lin, H., Wang, M., Duan, Y., Fu, Q., Ji, W., Cui, H., Jin, D., Lin, Y. and Hu, K.: O₃ sensitivity and contributions of different nmhc sources in O₃ formation at urban and suburban sites in Shanghai, *Atmosphere (Basel)*, 11(3), 295, 2020.
- Ling, Z. H., Guo, H., Cheng, H. R. and Yu, Y. F.: Sources of ambient volatile organic compounds and their contributions to photochemical ozone formation at a site in the Pearl River Delta, southern China, *Environ. Pollut.*, 159(10), 2310–2319, doi:10.1016/j.envpol.2011.05.001, 2011.
- Liu, X., Lyu, X., Wang, Y., Jiang, F. and Guo, H.: Intercomparison of O₃ formation and radical chemistry in the past decade at a suburban site in Hong Kong, *Atmos. Chem. Phys.*, 19(7), 5127–5145, doi:10.5194/acp-19-5127-2019, 2019a.
- Liu, X., Lyu, X., Wang, Y., Jiang, F. and Guo, H.: Intercomparison of O₃ formation and radical chemistry in the past decade at a suburban site in Hong Kong, *Atmos. Chem. Phys.*, 19(7), 5127–5145, doi:10.5194/acp-19-5127-2019, 2019b.
- Liu, X., Wang, N., Lyu, X., Zeren, Y., Jiang, F., Wang, X., Zou, S., Ling, Z. and Guo, H.: Photochemistry of ozone pollution in autumn in Pearl River Estuary, South China, *Sci. Total Environ.*, 754, 141812, doi:https://doi.org/10.1016/j.scitotenv.2020.141812, 2021a.



- 661 Liu, X., Wang, N., Lyu, X., Zeren, Y., Jiang, F., Wang, X., Zou, S., Ling, Z. and Guo,
 662 H.: Photochemistry of ozone pollution in autumn in Pearl River Estuary, South
 663 China, *Sci. Total Environ.*, 754, doi:10.1016/j.scitotenv.2020.141812, 2021b.
- 664 Lu, H., Lyu, X., Cheng, H., Ling, Z., Guo, H. and Lu, H.: Overview on the spatial–
 665 temporal characteristics of the ozone formation regime in China, *Environ. Sci.*, v.
 666 21(6), 916–929–2019 v.21 no.6, doi:10.1039/c9em00098d, 2019.
- 667 Lu, K., Zhang, Y., Su, H., Brauers, T., Chou, C. C., Hofzumahaus, A., Liu, S. C., Kita,
 668 K., Kondo, Y., Shao, M., Wahner, A., Wang, J., Wang, X. and Zhu, T.: Oxidant
 669 (O₃ + NO₂) production processes and formation regimes in Beijing, *J. Geophys.*
 670 *Res. Atmos.*, 115(7), 1–18, doi:10.1029/2009JD012714, 2010a.
- 671 Lu, K., Zhang, Y., Su, H., Shao, M., Zeng, L., Zhong, L., Xiang, Y., Chang, C., Chou,
 672 C. K. C. and Wahner, A.: Regional ozone pollution and key controlling factors of
 673 photochemical ozone production in Pearl River Delta during summer time, *Sci.*
 674 *China Chem.*, 53(3), 651–663, doi:10.1007/s11426-010-0055-6, 2010b.
- 675 Lu, X., Hong, J., Zhang, L., Cooper, O. R., Schultz, M. G., Xu, X., Wang, T., Gao, M.,
 676 Zhao, Y. and Zhang, Y.: Severe Surface Ozone Pollution in China: A Global
 677 Perspective, *Environ. Sci. Technol. Lett.*, 5(8), 487–494,
 678 doi:10.1021/acs.estlett.8b00366, 2018.
- 679 Lyu, X., Wang, N., Guo, H., Xue, L., Jiang, F., Zeren, Y., Cheng, H., Cai, Z., Han, L.
 680 and Zhou, Y.: Causes of a continuous summertime O₃ pollution event in Jinan, a
 681 central city in the North China Plain, *Atmos. Chem. Phys.*, 19(5), 3025–3042,
 682 doi:10.5194/acp-19-3025-2019, 2019a.
- 683 Lyu, X., Wang, N., Guo, H., Xue, L., Jiang, F., Zeren, Y., Cheng, H., Cai, Z., Han, L.
 684 and Zhou, Y.: Causes of a continuous summertime O₃ pollution event in Jinan, a
 685 central city in the North China Plain, *Atmos. Chem. Phys.*, 19(5), 3025–3042,
 686 doi:10.5194/acp-19-3025-2019, 2019b.
- 687 Lyu, X. P., Chen, N., Guo, H., Zhang, W. H., Wang, N., Wang, Y. and Liu, M.: Ambient
 688 volatile organic compounds and their effect on ozone production in Wuhan, central
 689 China, *Sci. Total Environ.*, 541, 200–209,
 690 doi:https://doi.org/10.1016/j.scitotenv.2015.09.093, 2016a.
- 691 Lyu, X. P., Chen, N., Guo, H., Zhang, W. H., Wang, N., Wang, Y. and Liu, M.: Ambient
 692 volatile organic compounds and their effect on ozone production in Wuhan, central
 693 China, *Sci. Total Environ.*, 541, 200–209, doi:10.1016/j.scitotenv.2015.09.093,
 694 2016b.
- 695 Qin, M., Chen, Z., Shen, H., Li, H., Wu, H. and Wang, Y.: Impacts of heterogeneous
 696 reactions to atmospheric peroxides: Observations and budget analysis study,
 697 *Atmos. Environ.*, 183(April), 144–153, doi:10.1016/j.atmosenv.2018.04.005,
 698 2018.
- 699 Saunders, S. M., Jenkin, M. E., Derwent, R. G. and Pilling, M. J.: Protocol for the
 700 development of the Master Chemical Mechanism, MCM v3 (Part A):
 701 Tropospheric degradation of non-aromatic volatile organic compounds, *Atmos.*
 702 *Chem. Phys.*, 3(1), 161–180, doi:10.5194/acp-3-161-2003, 2003.



- 703 Sillman, S.: Observation-Based Methods (OBMS) For Analyzing Urban/Regional
 704 Ozone Production And Ozone-NO_x-VOC Sensitivity, , (x), 1–44 [online]
 705 Available from: <http://www-personal.engin.umich.edu/~sillman>, 2010.
- 706 Stockwell, W. R., Kirchner, F., Kuhn, M. and Seefeld, S.: A new mechanism for
 707 regional atmospheric chemistry modeling, *J. Geophys. Res. Atmos.*, 102(22),
 708 doi:10.1029/97jd00849, 1997.
- 709 Stockwell, W. R., Saunders, E., Goliff, W. S. and Fitzgerald, R. M.: A perspective on
 710 the development of gas-phase chemical mechanisms for Eulerian air quality
 711 models, *J. Air Waste Manage. Assoc.*, 70(1), 44–70, 2020.
- 712 Su, R., Lu, K., Yu, J., Tan, Z., Jiang, M., Li, J., Xie, S., Wu, Y., Zeng, L. and Zhai, C.:
 713 Exploration of the formation mechanism and source attribution of ambient ozone
 714 in Chongqing with an observation-based model, *Sci. China Earth Sci.*, 61(1), 23–
 715 32, 2018a.
- 716 Su, R., Lu, K. D., Yu, J. Y., Tan, Z. F., Jiang, M. Q., Li, J., Xie, S. D., Wu, Y. S., Zeng,
 717 L. M., Zhai, C. Z. and Zhang, Y. H.: Exploration of the formation mechanism and
 718 source attribution of ambient ozone in Chongqing with an observation-based
 719 model, *Sci. China Earth Sci.*, 61(1), 23–32, doi:10.1007/s11430-017-9104-9,
 720 2018b.
- 721 Sun, L., Xue, L., Wang, T., Gao, J., Ding, A., Cooper, O. R., Lin, M., Xu, P., Wang, Z.,
 722 Wang, X., Wen, L., Zhu, Y., Chen, T., Yang, L., Wang, Y., Chen, J. and Wang,
 723 W.: Significant increase of summertime ozone at Mount Tai in Central Eastern
 724 China, *Atmos. Chem. Phys.*, 16(16), 10637–10650, doi:10.5194/acp-16-10637-
 725 2016, 2016.
- 726 Tan, Z., Lu, K., Dong, H., Hu, M., Li, X., Liu, Y., Lu, S., Shao, M., Su, R. and Wang,
 727 H.: Explicit diagnosis of the local ozone production rate and the ozone-NO_x-VOC
 728 sensitivities, *Sci. Bull.*, 63(16), 1067–1076, 2018a.
- 729 Tan, Z., Lu, K., Jiang, M., Su, R., Dong, H., Zeng, L., Xie, S., Tan, Q. and Zhang, Y.:
 730 Exploring ozone pollution in Chengdu, southwestern China: A case study from
 731 radical chemistry to O₃-VOC-NO_x sensitivity, *Sci. Total Environ.*, 636, 775–786,
 732 2018b.
- 733 Tan, Z., Lu, K., Jiang, M., Su, R., Wang, H., Lou, S., Fu, Q., Zhai, C., Tan, Q. and Yue,
 734 D.: Daytime atmospheric oxidation capacity in four Chinese megacities during the
 735 photochemically polluted season: a case study based on box model simulation,
 736 *Atmos. Chem. Phys.*, 19(6), 3493–3513, 2019a.
- 737 Tan, Z., Lu, K., Jiang, M., Su, R., Wang, H., Lou, S., Fu, Q., Zhai, C., Tan, Q., Yue, D.,
 738 Chen, D., Wang, Z., Xie, S., Zeng, L. and Zhang, Y.: Daytime atmospheric
 739 oxidation capacity in four Chinese megacities during the photochemically polluted
 740 season: A case study based on box model simulation, *Atmos. Chem. Phys.*, 19(6),
 741 3493–3513, doi:10.5194/acp-19-3493-2019, 2019b.
- 742 Vingarzan, R.: A review of surface ozone background levels and trends, *Atmos.*
 743 *Environ.*, 38(21), 3431–3442, 2004.
- 744 Wang, H., Hu, X. and Sterba-Boatwright, B.: A new statistical approach for interpreting



- oceanic fCO₂ data, *Mar. Chem.*, 183, 41–49, 2016.
- Wang, M., Hu, K., Chen, W., Shen, X., Li, W. and Lu, X.: Ambient Non-Methane Hydrocarbons (NMHCs) Measurements in Baoding, China: Sources and Roles in Ozone Formation, *Atmosphere (Basel)*, 11(11), 1205, 2020a.
- Wang, P., Chen, Y., Hu, J., Zhang, H. and Ying, Q.: Attribution of Tropospheric Ozone to NO_x and VOC Emissions: Considering Ozone Formation in the Transition Regime, *Environ. Sci. Technol.*, 53(3), 1404–1412, doi:10.1021/acs.est.8b05981, 2019.
- Wang, T., Xue, L., Brimblecombe, P., Lam, Y. F., Li, L. and Zhang, L.: Ozone pollution in China: A review of concentrations, meteorological influences, chemical precursors, and effects, *Sci. Total Environ.*, 575, 1582–1596, doi:10.1016/j.scitotenv.2016.10.081, 2017a.
- Wang, T., Xue, L., Brimblecombe, P., Lam, Y. F., Li, L. and Zhang, L.: Ozone pollution in China: A review of concentrations, meteorological influences, chemical precursors, and effects, *Sci. Total Environ.*, 575, 1582–1596, 2017b.
- Wang, W., Yuan, B., Peng, Y., Su, H., Cheng, Y., Yang, S., Wu, C., Qi, J., Bao, F. and Huangfu, Y.: Direct observations indicate photodegradable oxygenated volatile organic compounds (OVOCs) as larger contributors to radicals and ozone production in the atmosphere, *Atmos. Chem. Phys.*, 22(6), 4117–4128, 2022.
- Wang, Y., Wang, H., Guo, H., Lyu, X., Cheng, H., Ling, Z., Louie, P. K. K., Simpson, I. J., Meinardi, S. and Blake, D. R.: Long-term O₃-precursor relationships in Hong Kong: field observation and model simulation, *Atmos. Chem. Phys.*, 17(18), 10919–10935, 2017c.
- Wang, Y., Wang, H., Guo, H., Lyu, X., Cheng, H., Ling, Z., Louie, P. K. K., Simpson, I. J., Meinardi, S. and Blake, D. R.: Long-term O₃-precursor relationships in Hong Kong: Field observation and model simulation, *Atmos. Chem. Phys.*, 17(18), 10919–10935, doi:10.5194/acp-17-10919-2017, 2017d.
- Wang, Y., Guo, H., Zou, S., Lyu, X., Ling, Z., Cheng, H. and Zeren, Y.: Surface O₃ photochemistry over the South China Sea: Application of a near-explicit chemical mechanism box model, *Environ. Pollut.*, 234, 155–166, doi:10.1016/j.envpol.2017.11.001, 2018.
- Wang, Y., Gao, W., Wang, S., Song, T., Gong, Z., Ji, D., Wang, L., Liu, Z., Tang, G., Huo, Y., Tian, S., Li, J., Li, M., Yang, Y., Chu, B., Petäjä, T., Kerminen, V. M., He, H., Hao, J., Kulmala, M., Wang, Y. and Zhang, Y.: Contrasting trends of PM_{2.5} and surface-ozone concentrations in China from 2013 to 2017, *Natl. Sci. Rev.*, 7(8), 1331–1339, doi:10.1093/nsr/nwaa032, 2020b.
- Whalley, L. K., Slater, E. J., Woodward-Massey, R., Ye, C., Lee, J. D., Squires, F., Hopkins, J. R., Dunmore, R. E., Shaw, M. and Hamilton, J. F.: Evaluating the sensitivity of radical chemistry and ozone formation to ambient VOCs and NO_x in Beijing, *Atmos. Chem. Phys.*, 21(3), 2125–2147, 2021a.
- Whalley, L. K., Slater, E. J., Woodward-Massey, R., Ye, C., Lee, J. D., Squires, F., Hopkins, J. R., Dunmore, R. E., Shaw, M., Hamilton, J. F., Lewis, A. C., Mehra,



- 787 A., Worrall, S. D., Bacak, A., Bannan, T. J., Coe, H., Percival, C. J., Ouyang, B.,
 788 Jones, R. L., Crilley, L. R., Kramer, L. J., Bloss, W. J., Vu, T., Kotthaus, S.,
 789 Grimmond, S., Sun, Y., Xu, W., Yue, S., Ren, L., Joe, W., Nicholas Hewitt, C.,
 790 Wang, X., Fu, P. and Heard, D. E.: Evaluating the sensitivity of radical chemistry
 791 and ozone formation to ambient VOCs and NO_x in Beijing, *Atmos. Chem. Phys.*,
 792 21(3), 2125–2147, doi:10.5194/acp-21-2125-2021, 2021b.
- 793 Willmott, C. J.: Some comments on the evaluation of model performance., *Bull. - Am.*
 794 *Meteorol. Soc.*, 63(11), 1309–1313, doi:10.1175/1520-
 795 0477(1982)063<1309:SCOTEO>2.0.CO;2, 1982.
- 796 Wolfe, G. M., Thornton, J. A., Bouvier-Brown, N. C., Goldstein, A. H., Park, J.-H.,
 797 McKay, M., Matross, D. M., Mao, J., Brune, W. H. and LaFranchi, B. W.: The
 798 Chemistry of Atmosphere-Forest Exchange (CAFE) model–part 2: application to
 799 BEARPEX-2007 observations, *Atmos. Chem. Phys.*, 11(3), 1269–1294, 2011.
- 800 Wolfe, G. M., Marvin, M. R., Roberts, S. J., Travis, K. R. and Liao, J.: The framework
 801 for 0-D atmospheric modeling (F0AM) v3. 1, *Geosci. Model Dev.*, 9(9), 3309–
 802 3319, 2016.
- 803 Xie, X., Shao, M., Liu, Y., Lu, S., Chang, C.-C. and Chen, Z.-M.: Estimate of initial
 804 isoprene contribution to ozone formation potential in Beijing, China, *Atmos.*
 805 *Environ.*, 42(24), 6000–6010, 2008.
- 806 Xu, Z., Huang, X., Nie, W., Chi, X., Xu, Z., Zheng, L., Sun, P. and Ding, A.: Influence
 807 of synoptic condition and holiday effects on VOCs and ozone production in the
 808 Yangtze River Delta region, China, *Atmos. Environ.*, 168, 112–124, 2017.
- 809 Xue, L., Wang, T., Louie, P. K. K., Luk, C. W. Y., Blake, D. R. and Xu, Z.: Increasing
 810 external effects negate local efforts to control ozone air pollution: a case study of
 811 Hong Kong and implications for other Chinese cities, *Environ. Sci. Technol.*,
 812 48(18), 10769–10775, 2014a.
- 813 Xue, L., Wang, T., Louie, P. K. K., Luk, C. W. Y., Blake, D. R. and Xu, Z.: Increasing
 814 external effects negate local efforts to control ozone air pollution: A case study of
 815 Hong Kong and implications for other chinese cities, *Environ. Sci. Technol.*,
 816 48(18), 10769–10775, doi:10.1021/es503278g, 2014b.
- 817 Xue, L. K., Wang, T., Gao, J., Ding, A. J., Zhou, X. H., Blake, D. R., Wang, X. F.,
 818 Saunders, S. M., Fan, S. J., Zuo, H. C., Zhang, Q. Z. and Wang, W. X.: Ground-
 819 level ozone in four Chinese cities: Precursors, regional transport and
 820 heterogeneous processes, *Atmos. Chem. Phys.*, 14(23), 13175–13188,
 821 doi:10.5194/acp-14-13175-2014, 2014c.
- 822 Xue, M., Ma, J., Tang, G., Tong, S., Hu, B., Zhang, X., Li, X. and Wang, Y.: RO_x
 823 Budgets and O₃ Formation during Summertime at Xianghe Suburban Site in the
 824 North China Plain, *Adv. Atmos. Sci.*, 38(7), 1209–1222, 2021.
- 825 Xue, T., Zheng, Y., Geng, G., Xiao, Q., Meng, X., Wang, M., Li, X., Wu, N., Zhang,
 826 Q. and Zhu, T.: Estimating Spatiotemporal Variation in Ambient Ozone Exposure
 827 during 2013–2017 Using a Data-Fusion Model, *Environ. Sci. Technol.*, 54(23),
 828 14877–14888, 2020.



- 829 Yarwood, G., Rao, S., Yocke, M. and Whitten, G. Z.: Updates to the carbon bond
 830 chemical mechanism: CB05, Final Rep. to US EPA, RT-0400675, 8, 13, 2005.
- 831 Yarwood, G., Jung, J., Whitten, G. Z., Heo, G., Mellberg, J. and Estes, M.: Updates to
 832 the Carbon Bond mechanism for version 6 (CB6), in 9th Annual CMAS
 833 Conference, Chapel Hill, NC, pp. 11–13., 2010.
- 834 Yin, M., Zhang, X., Li, Y., Fan, K., Li, H., Gao, R. and Li, J.: Ambient ozone pollution
 835 at a coal chemical industry city in the border of Loess Plateau and Mu Us Desert:
 836 characteristics, sensitivity analysis and control strategies, *PeerJ*, 9, e11322, 2021.
- 837 Yu, D., Tan, Z., Lu, K., Ma, X., Li, X., Chen, S., Zhu, B., Lin, L., Li, Y., Qiu, P., Yang,
 838 X., Liu, Y., Wang, H., He, L., Huang, X. and Zhang, Y.: An explicit study of local
 839 ozone budget and NO_x-VOCs sensitivity in Shenzhen China, *Atmos. Environ.*,
 840 224, 117304, doi:https://doi.org/10.1016/j.atmosenv.2020.117304, 2020a.
- 841 Yu, D., Tan, Z., Lu, K., Ma, X., Li, X., Chen, S., Zhu, B., Lin, L., Li, Y., Qiu, P., Yang,
 842 X., Liu, Y., Wang, H., He, L., Huang, X. and Zhang, Y.: An explicit study of local
 843 ozone budget and NO_x-VOCs sensitivity in Shenzhen China, *Atmos. Environ.*,
 844 224(November 2019), 117304, doi:10.1016/j.atmosenv.2020.117304, 2020b.
- 845 Zeng, L., Lyu, X., Guo, H., Zou, S. and Ling, Z.: Photochemical Formation of C1–C5
 846 Alkyl Nitrates in Suburban Hong Kong and over the South China Sea, *Environ.*
 847 *Sci. Technol.*, 52(10), 5581–5589, doi:10.1021/acs.est.8b00256, 2018.
- 848 Zhang, Q., Zheng, Y., Tong, D., Shao, M., Wang, S., Zhang, Y., Xu, X., Wang, J., He,
 849 H., Liu, W., Ding, Y., Lei, Y., Li, J., Wang, Z., Zhang, X., Wang, Y., Cheng, J.,
 850 Liu, Y., Shi, Q., Yan, L., Geng, G., Hong, C., Li, M., Liu, F., Zheng, B., Cao, J.,
 851 Ding, A., Gao, J., Fu, Q., Huo, J., Liu, B., Liu, Z., Yang, F., He, K. and Hao, J.:
 852 Drivers of improved PM_{2.5} air quality in China from 2013 to 2017, *Proc. Natl.*
 853 *Acad. Sci.*, 116(49), 24463 LP – 24469, doi:10.1073/pnas.1907956116, 2019.
- 854 Zhang, Y., Xue, L., Carter, W. P. L., Pei, C., Chen, T., Mu, J., Wang, Y., Zhang, Q. and
 855 Wang, W.: Development of ozone reactivity scales for volatile organic
 856 compounds in a Chinese megacity, *Atmos. Chem. Phys.*, 21(14), 11053–11068,
 857 doi:10.5194/acp-21-11053-2021, 2021.
- 858 Zhang, Y. H., Hu, M., Zhong, L. J., Wiedensohler, A., Liu, S. C., Andreae, M. O., Wang,
 859 W. and Fan, S. J.: Regional Integrated Experiments on Air Quality over Pearl
 860 River Delta 2004 (PRIDE-PRD2004): Overview, *Atmos. Environ.*, 42(25), 6157–
 861 6173, doi:10.1016/j.atmosenv.2008.03.025, 2008a.
- 862 Zhang, Y. H., Su, H., Zhong, L. J., Cheng, Y. F., Zeng, L. M., Wang, X. S., Xiang, Y.
 863 R., Wang, J. L., Gao, D. F., Shao, M., Fan, S. J. and Liu, S. C.: Regional ozone
 864 pollution and observation-based approach for analyzing ozone–precursor
 865 relationship during the PRIDE-PRD2004 campaign, *Atmos. Environ.*, 42(25),
 866 6203–6218, doi:https://doi.org/10.1016/j.atmosenv.2008.05.002, 2008b.
- 867 Zhao, Y., Chen, L., Li, K., Han, L., Zhang, X., Wu, X., Gao, X., Azzi, M. and Cen, K.:
 868 Atmospheric ozone chemistry and control strategies in Hangzhou, China:
 869 Application of a 0-D box model, *Atmos. Res.*, 246, 105109, 2020.
- 870 Zong, R., Yang, X., Wen, L., Xu, C., Zhu, Y., Chen, T., Yao, L., Wang, L., Zhang, J.,



871 Yang, L., Wang, X., Shao, M., Zhu, T., Xue, L. and Wang, W.: Strong ozone
872 production at a rural site in theNorth China Plain: Mixed effects of urban
873 plumesand biogenic emissions, J. Environ. Sci. (China), 71, 261–270,
874 doi:10.1016/j.jes.2018.05.003, 2018.
875

876 **Table 1.** Summary of published 0-D box model studies in China

City	Site/Type	Period	Patterns of Time scale ^a	Mechanism	Reference
Beijing	PKU ^b	Urban	10 Aug–10 Sep 2006	Day-to-day (25 d)	CB-IV (Lu et al., 2010)
	YUFA	Suburban			
Beijing	PKU	Urban	13–29 Apr 2015, 11–29 Aug 2015, 22 Feb–12 Mar 2016	Entire period	RACM2 (Qin et al., 2018)
	Beijing	Urban	2–19 Jul 2014	Entire period	RACM2 (Tan et al., 2019b)
Dezhou	Yucheng	Rural	1 Jun–6 Jul 2013	Day-to-day (2 d)	MCMV3.3.1 (Zong et al., 2018)
Shenzhen	SY ^c	Urban	28 Sep–31 Oct 2018	Entire period	RACM2 (Yu et al., 2020b)
	Fucheng	Urban			
Hong Kong	TC	Suburban	10 Aug–21 Oct 2013	Entire period	MCMV3.2 (Zeng et al., 2018)
	Wan Shan	Island			
	Tung Chung	Urban	Sep–Nov 2002, 2007, 2012	Year-to-year (3 yrs)	MCMV3.2 (Xue et al., 2014b)
	Qing Sha	Urban	23 Oct–1 Nov 2007	Day-to-day (10 d)	CB-IV (Cheng et al., 2010)
Tung Chung	Tai O	Urban	Jan 2005–Dec 2014	Month-to-month (5 months)	CB05 (Whalley et al., 2021b)
	Tung Chung	Urban			
Chengdu	Pengzhou	Suburban			
	Pixian	Suburban			
	Shuangliu	Suburban	3 Sep–2 Oct 2016	Entire period	RACM2 (Tan et al., 2018b)
Chengdu	Chengzhong	Urban			
	Chengzhong	Urban			
Zhuhai	Qi'ao	Mountain	25 Sep–28 Oct 2016	Entire period	MCMV3.2 (Liu et al., 2021b)
Wuhan	HPMC ^d	Urban	Feb 2013–Oct 2014	Month-to-month (21 months)	MCMV3.2 (Lyu et al., 2016)
Guangzhou	GZ	Urban	5–17 Jul 2006	Day-to-day (16 d)	CB-IV (Lu et al., 2010)
	BZ	Suburban			
	Guangzhou	Urban			
	Xinken	Nonurban	4 Oct–5 Nov 2004	Entire period	SAPRC (Zhang et al., 2008b)
Hangzhou	Zhaohui	Urban	17 May, 26 Jun 20, Jul 24, Aug	Entire period (5 d)	MCMV3.3.1 (Zhao et al., 2020)
	Xiasha	Suburban	and 26 Sep		





	Huapu	Urban					
Nanjing	NUIST ^e	Suburban	3 Jul–1 Aug 2018	Entire period	CB-IV	(Fan et al., 2021)	
	SORPES	Suburban	22 Sep–7 Oct 2014	Day-to-day (8 d)	MCMv3.3.1	(Xu et al., 2017)	
Yulin	EMB ^f	Urban	7 Jul–10 Aug 2019	Day-to-day (13 d)	MCMv3.3.1	(Yin et al., 2021)	
Lanzhou	Renshoushan Park	Urban	19 Jun–16 Jul 2006	Day-to-day (3 d)	MCMv3.2	(Xue et al., 2014)	
Baoding	EPB ^g	Urban	10–30 Sep 2015	Day-to-day (5 d)	MCMv3.3.1	(Wang et al., 2020a)	
Chongqing	Nan Quan	Suburban					
	Chao Zhan	Urban	24 Aug–22 Sep 2015	Day-to-day (7 d)	MCMv3.2	(Li et al., 2018)	
	Jin Yun Shan	Urban					
Shanghai	Pudong	Urban	1–31 Jul 2017	Day-to-day (16 d)	CB-IV	(Lin et al., 2020)	
	Dianshanhu	Suburban					
South China Sea	Wanshan	Island	11 Sep–21 Nov 2013	Entire period	MCMv3.2	(Wang et al., 2018)	

^aNumber of days for modeling the patterns of time scale denotes that which was simulated by the box model.

^bPeking University

^cShenzhen Yanjiusheng Yuan

^dHubei Provincial Environmental Monitoring Center

^eNanjing University of Information Science & Technology

^fEnvironmental Monitoring Building

^gEnvironmental Protection Bureau

^aNumber of days for modeling the patterns of time scale denotes that which was simulated by the box model.

^bPeking University

^cShenzhen Yanjusheng Yuan

^dHubei Provincial Environmental Monitoring Center

^eNanjing University of Information Science & Technology

^fEnvironmental Monitoring Building

^gEnvironmental Protection Bureau



Table 2. Summary of the number of days (for model calculation) and proportions that were classified into the three photochemical regimes across each site and multiple patterns of time scale.

Patterns of Time scale	Site	Photochemical regime: RIR_{NOx}/RIR_{AVOC}					
		NO _x -limited: >2		Transition: 0.5~2		VOC-limited: <0.5	
		No. of days	Proportion	No. of days	Proportion	No. of days	Proportion
Month-to-month	TZ	2	40%	2	40%	1	20%
	BJ	0	0%	3	60%	2	40%
	XD	0	0%	2	40%	3	60%
Week-to-week	TZ	7	33%	8	38%	6	29%
	BJ	0	0%	10	50%	10	50%
	XD	3	16%	6	32%	10	53%
Day-to-day	TZ	29	29%	45	45%	26	26%
	BJ	0	0%	21	26%	60	74%
	XD	20	18%	23	20%	71	62%

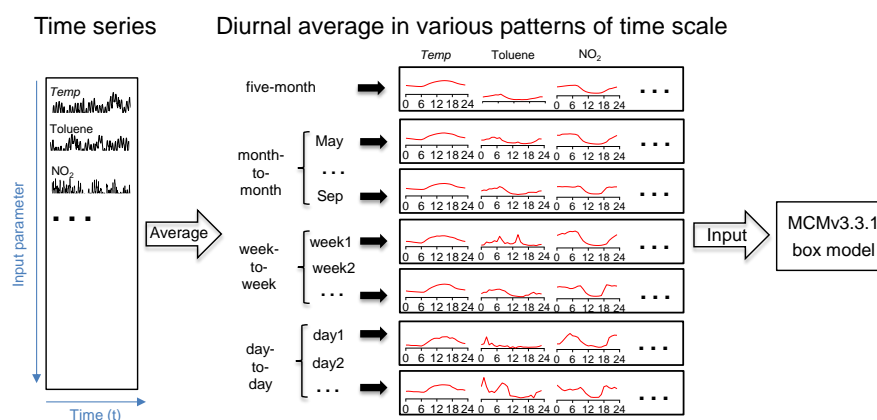


Figure 1. Schematic diagram of the dataset treatment to derive four patterns of time scale for 0-D box model input. Note that the four patterns (i.e., five-month, monthly, weekly, and daily) were the diurnal average of the initial dataset. This diagram takes one site and several input measurements (temperature, toluene, and NO₂) as examples.

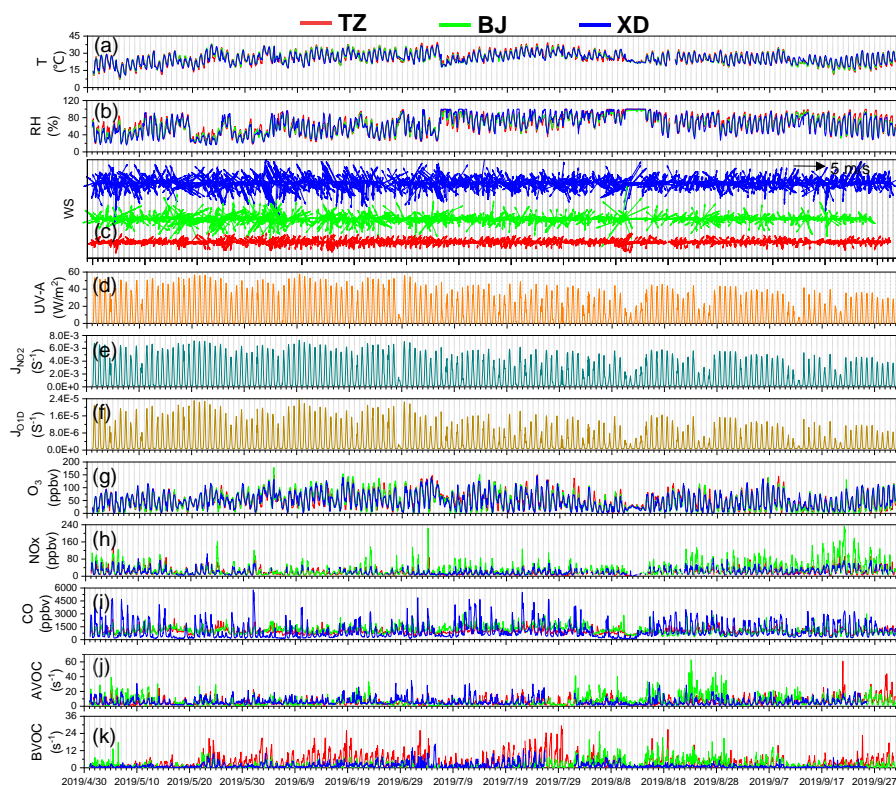
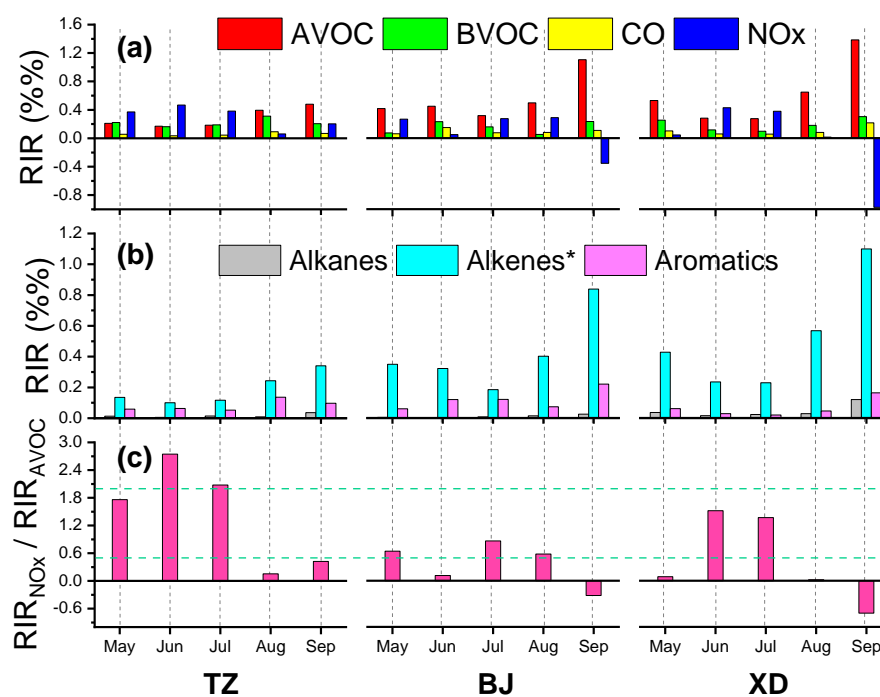


Figure 2. Time series of meteorological parameters, O_3 and its precursors (i.e., CO, NO_x, VOCs) throughout the whole campaign at the three sites in Zibo.



890

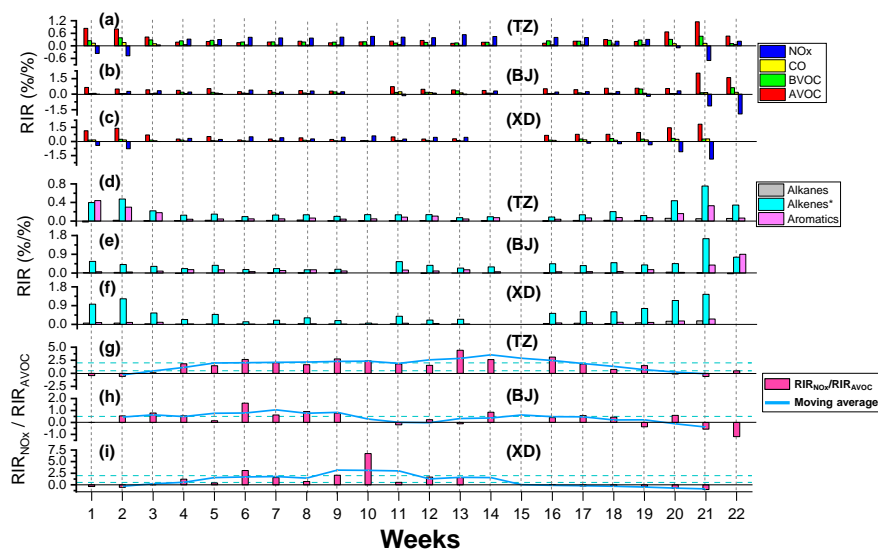


891

892 **Figure 3.** Time series of month-to-month RIR values of major precursor groups and RIR_{NOx}/RIR_{AVOC} at
 893 three sites (TZ, BJ and XD) in Zibo. The green dash line indicates to $RIR_{NOx}/RIR_{AVOC} = 0.5$ and 2.



894



895
 896 **Figure 4.** Time series of week-to-week RIR values of major precursor groups and RIR_{NOx}/RIR_{AVOC} at
 897 three sites (TZ, BJ, and XD) in Zibo. The blue lines in (g)-(i) are the three points moving average of
 898 RIR_{NOx}/RIR_{AVOC} value.

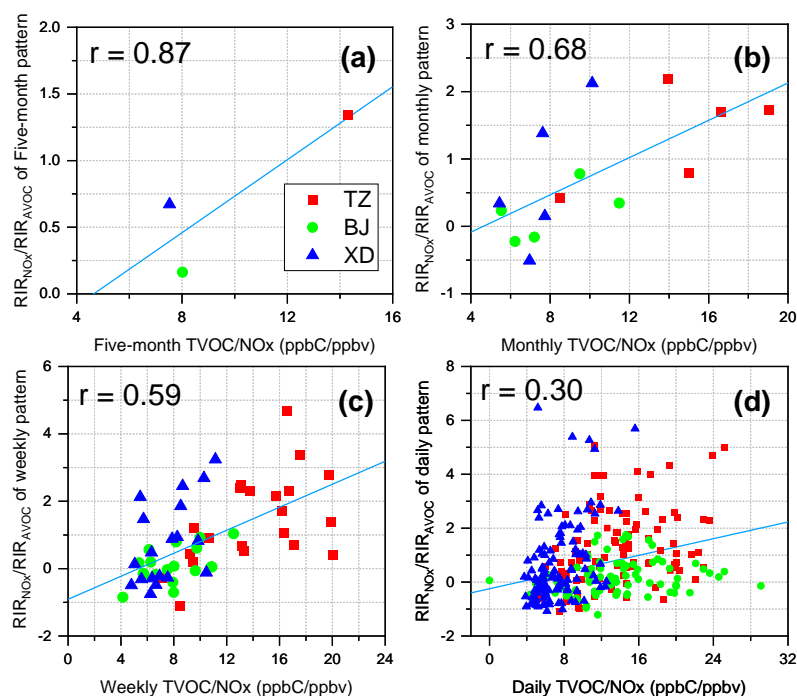
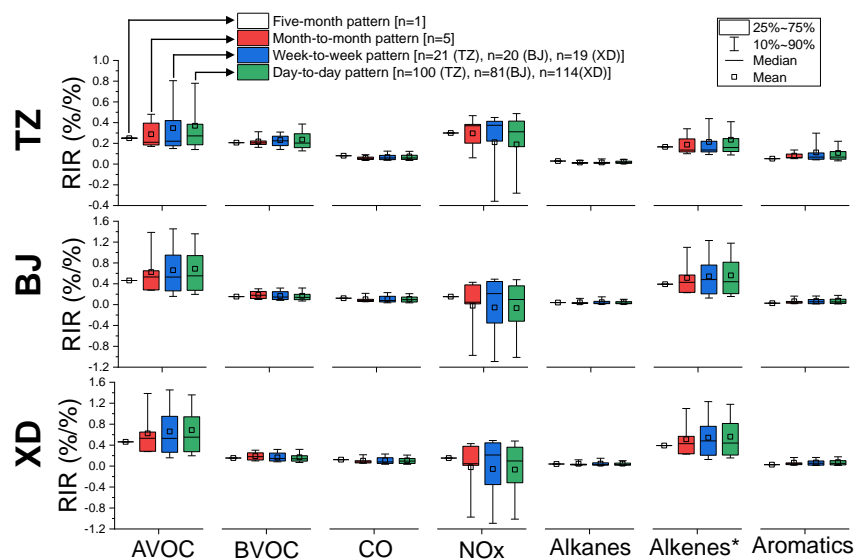


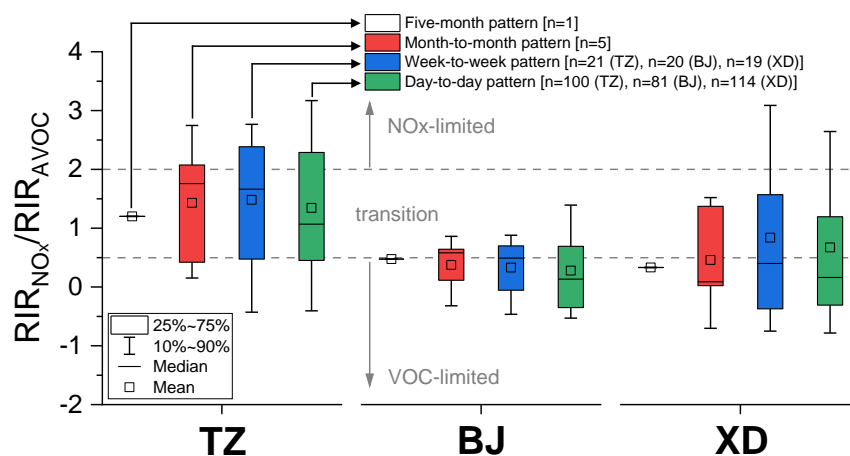
Figure 5. The correlations of TVOC/NOx with RIR_{NOx}/RIR_{AVOC} at multiple patterns of time scale at the three sites in Zibo.



902



903
 904 **Figure 6.** Distribution of RIR values of major precursor groups in multiple patterns of time scale at three
 905 sites (TZ, BJ, and XD) in Zibo.



906

907 **Figure 7.** Distribution of RIR_{NOx}/RIR_{AVOC} (indicator of photochemical regime) in multiple patterns of
 908 time scale at three sites (TZ, BJ, and XD) in Zibo.

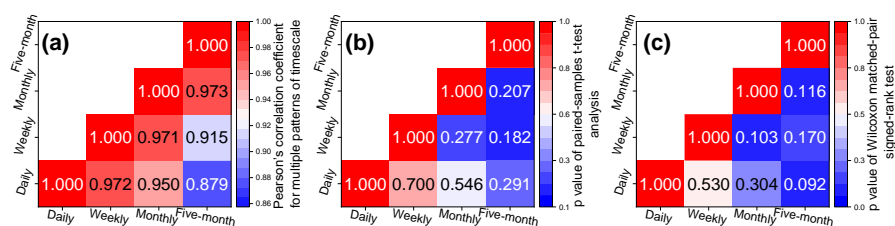


Figure 8. The statistical analysis results of RIR values (from Table S6) at multiple patterns of time scale: (a) Pearson's r correlation analysis (all the results have passed statistical significance assumed at $p < 0.01$), (b) Paired-samples t-test analysis (* p values refer to differences with a statistical significance assumes at $p < 0.05$), (c) Wilcoxon matched-pair signed-rank test (* p values refer to differences with a statistical significance assumes at $p < 0.05$).

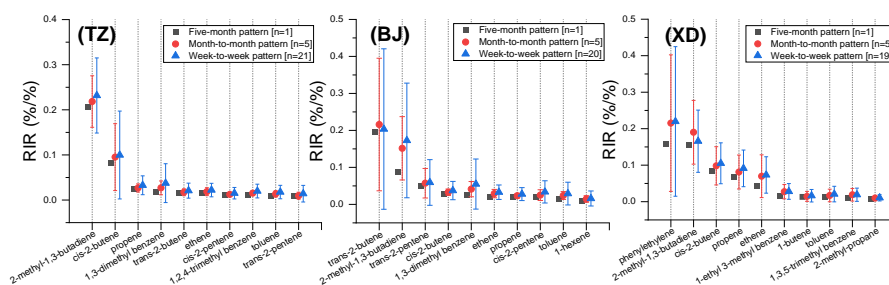
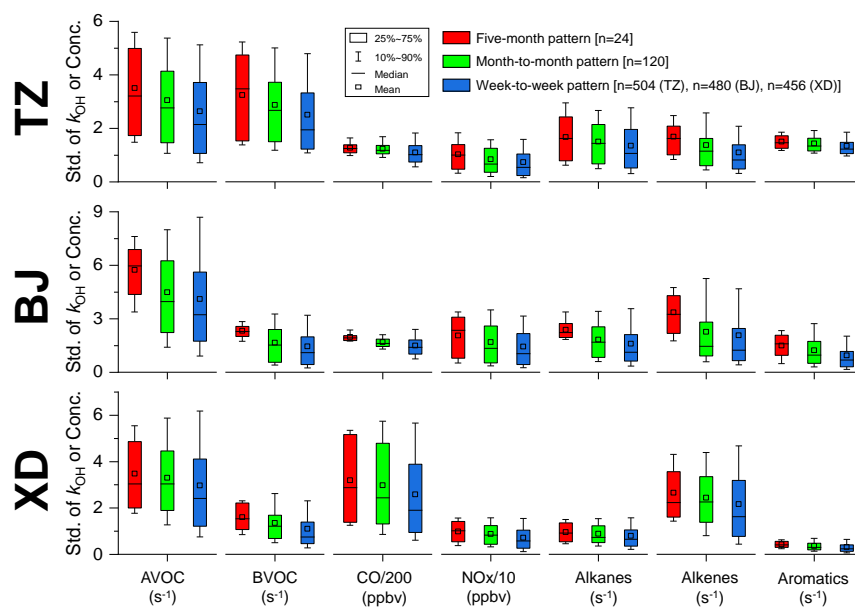


Figure 9. Averaged RIR values of individual AVOC species (top 10) at different patterns of time scale at three sites (TZ, BJ, and XD) in Zibo. The error bars represent the standard deviations of the mean.



918
 919 **Figure 10.** Distributions of the standard deviations (Std.) for OH reactivity (k_{OH}) or concentration of O_3
 920 precursor groups for multiple patterns of time scale at the three sites in Zibo. For example, there would
 921 be 24 standard deviation values when averaging into five-month diurnal pattern; and months \times 24 standard
 922 deviation values ($n=120$ for all sites) when averaging into monthly pattern; and weeks \times 24 standard
 923 deviation values ($n=504, 480, 456$ for TZ, BJ, XD) when averaging into weekly pattern.